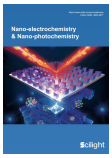
Nano-electrochemistry & Nano-photochemistry
https://www.sciltp.com/journals/nenp



Article

Three-Dimensional Pyrrolo[3,2-*b*]pyrrole-Based Covalent Organic Polymers for Continuous H_2O_2 Production

Xiaoyi Yue, Hao Chen, Shangrui Wu, Yingguo Li *, Danfeng Jiang, Xiao Chen and Chao Yu *

School of Environmental and Chemical Engineering, Jiangsu University of Science and Technology, Zhenjiang 212100, China
* Correspondence: liyg2022@just.edu.cn (Y.L.); chao_yu@just.edu.cn (C.Y.)

How To Cite: Yue, X.; Chen, H.; Wu, S.; et al. Three-Dimensional Pyrrolo[3,2-*b*]pyrrole-Based Covalent Organic Polymers for Continuous H_2O_2 Production. *Nano-electrochemistry & Nano-photochemistry* **2026**, *2*(4), 26. https://doi.org/10.53941/nenp.2026.100026

Received: 5 September 2026
Revised: 30 October 2026
Accepted: 10 November 2026
Published: 20 November 2026

Abstract: Photocatalytic hydrogen peroxide (H_2O_2) synthesis is often hindered by rapid charge recombination and sluggish oxygen activation. Herein, we report a three-dimensional pyrrolo[3,2-*b*]pyrrole-based covalent organic polymer (PP-COP-**9**) synthesized via a multicomponent cyclization strategy. The nonplanar 3D framework effectively regulates excited-state charge dynamics, achieving a high H_2O_2 production rate of 5269 μmol g^{-1} h^{-1} in pure water. By introducing benzyl alcohol as a hole scavenger, the rate surges to 118,936 μmol g^{-1} h^{-1}, which is approximately 23 times higher than that in pure water due to efficient hole consumption and a favorable biphasic interface. Furthermore, PP-COP-**9** demonstrates excellent stability and is successfully integrated into a continuous-flow photoreactor to maintain a stable H_2O_2 concentration of ~21.36 mM for 8 h. This work highlights the critical role of 3D framework engineering in boosting photocatalytic efficiency for practical H_2O_2 production.

Keywords: covalent organic polymers; 3D framework engineering; photocatalytic hydrogen peroxide (H_2O_2) synthesis; oxygen reduction reaction; continuous flow

1. Introduction

Hydrogen peroxide (H_2O_2), as a green, mild, and environmentally benign oxidant, plays an indispensable role in modern chemical industries [1], healthcare [2], household chemicals [3], and textile processing [4]. However, the anthraquinone process, which currently dominates industrial H_2O_2 production, involves complex multistep procedures and intensive energy consumption, while also generating considerable organic by-products and carbon emissions, which conflicts with the overarching goals of sustainable development [5]. Although electrochemical H_2O_2 production offers a relatively straightforward and environmentally friendly route, its reliance on noble-metal catalysts and substantial electricity consumption severely restricts large-scale implementation [6,7]. Against this backdrop, photocatalysis has emerged as a promising sustainable alternative, enabling the direct synthesis of H_2O_2 from water and oxygen using solar energy [8–10].

However, the development of highly efficient photocatalysts for this process remains a formidable challenge. First, conventional inorganic photocatalysts, such as TiO_2 [11], ZnO [12], CdS [13], and C_3N_4 [14], often suffer from limited light-harvesting capabilities, with their photoresponse largely confined to the ultraviolet or short-wavelength visible-light regions, thereby restricting photocatalytic efficiency. Moreover, the generated H_2O_2 is susceptible to further decomposition on photocatalytic surfaces, further limiting its net accumulation [15–17]. In recent years, covalent organic polymers (COPs), owing to their structural tunability, adjustable electronic properties, and favorable optoelectronic characteristics, have emerged as promising metal-free photocatalysts for H_2O_2 production [18–23]. Current molecular engineering strategies mainly focus on extending π-conjugation, constructing donor-acceptor structures, introducing heteroatoms, and regulating linkage units to improve charge

Copyright: © 2026 by the authors. This is an open access article under the terms and conditions of the Creative Commons Attribution (CC BY) license (https://creativecommons.org/licenses/by/4.0/).
Publisher's Note: Scilight stays neutral with regard to jurisdictional claims in published maps and institutional affiliations.

separation and transfer [24–27]. However, these approaches predominantly emphasize chemical composition and electronic structure, while the role of framework dimensionality and spatial configuration in governing excited-state dynamics and interfacial reactions remains insufficiently understood [28–31]. In particular, conventional planar or quasi-two-dimensional conjugated frameworks may suffer from strong π-π stacking and unfavorable excited-state recombination [32–37]. Constructing three-dimensional conjugated frameworks therefore provides an alternative strategy to regulate spatial electronic coupling, charge-carrier dynamics, and reactant accessibility, potentially facilitating O_2 activation and suppressing the secondary consumption of H_2O_2.

Based on this consideration, a series of three-dimensional pyrrolo[3,2-*b*]pyrrole-based covalent organic polymers were constructed, and the relationship between framework configuration and photocatalytic H_2O_2 production was systematically investigated. Among them, the optimized PP-COP-**9** exhibits favorable light-harvesting capability, a suitable band structure, and prolonged excited-state lifetime, thereby facilitating photogenerated charge utilization and interfacial O_2 activation. PP-COP-**9** achieves an H_2O_2 production rate of 5269 μmol g^{-1} h^{-1} in pure water, which is further increased to 118,936 μmol g^{-1} h^{-1} upon the addition of benzyl alcohol (BA), benefiting from efficient hole scavenging and the favorable biphasic interfacial environment. Moreover, PP-COP-**9** maintains high photocatalytic activity in complex water matrices. Integration with a spiral-coil continuous-flow photoreactor further enables stable and continuous H_2O_2 production, maintaining an H_2O_2 concentration of approximately 21.36 mM under optimized conditions. This work establishes a structure–function relationship between the three-dimensional framework configuration, excited-state charge dynamics, and interfacial O_2 activation, highlighting three-dimensional framework engineering as an effective strategy for the development of efficient organic photocatalysts toward continuous H_2O_2 production.

2. Materials and Methods

2.1. Materials Characterization

2.1.1. Materials

All raw materials were purchased from Aladdin Corporation, and Shanghai Titan Scientific Co., Ltd. All commercial chemicals were used directly without further purification and the solvents were dried according to the standard methods.

2.1.2. Characterzation

Fourier transform infrared (FT-IR) spectra were obtained using a Bruker Tensor 37 infrared spectrometer (Bruker Optik GmbH, Ettlingen, Germany). ^{13}C cross-polarization magic angle spinning (CP/MAS) solid-state NMR spectroscopy was recorded on a 400 MHz WB solid-state NMR spectrometer. Scanning electron microscopy (SEM) images were obtained using a SU8010 electron microscope. Thermogravimetric analysis (TGA) was conducted using an SDTA851e thermo-analyzer. The X-ray analysis was performed. Photoelectron spectroscopy (XPS) was acquired using a Thermo Scientific K-Alpha spectrometer. Ultraviolet-visible diffuse reflectance absorption spectra (UV-Vis-DRS) were collected using a Shimadzu UV-2600 spectrophotometer. Electron paramagnetic resonance (EPR) spectra were obtained using a Bruker ELEXSYS II E 500 EPR spectrometer at room temperature.

2.1.3. Photoelectrochemical Characterization

Photochemical tests, including electrochemical impedance spectroscopy (EIS), photocurrent response, and Mott-Schottky plots were carried out on an electrochemical workstation (CHI660C, China) in a standard three-electrode system. The synthesised samples acted as the working electrodes, the Pt mesh (1 × 1 cm) acted as the counter electrode, and Ag/AgCl (saturated KCl) acted as the reference electrode. A 365 nm LED lamp was employed as the light source, while a Na_2SO_4 (0.1 mol L^{-1}) aqueous solution served as the electrolyte. The working electrodes were prepared as follows: 0.05 g photocatalyst was ground with 0.5 mL of ethanol to form a homogeneous slurry ink. Subsequently, the catalyst ink was coated onto an F-doped SnO_2-coated glass (FTO glass, 2 × 2 cm) substrate using the doctor blade technique. All investigated electrodes exhibited a similar film thickness of approximately 10 μm.

2.1.4. Spiral-Coiled Continuous-Flow Photocatalytic H_2O_2 Experiment

Deionized water (45 mL), benzyl alcohol (5 mL), and PP-COP-**9** (5 mg) were added to a beaker, followed by ultrasonication for 30 min to fully disperse the catalyst in the aqueous phase. Subsequently, the reaction mixture

was pumped using a syringe pump. During the gas phase introduction, the oxygen flow rate was adjusted using a gas mass flow meter. The gas and liquid streams were combined at a Y-shaped three-way junction. The gas-to-liquid flow ratios were varied at 3:1, 2:1, 1:1, 1:2 and 1:3, while the total flow rate was maintained at approximately 200 μL/min. Upon completion of the reaction, the catalyst was separated from the reaction mixture by centrifugation.

2.1.5. Thermogravimetric Analyses (TGA)

Thermal analysis was conducted using a SDTA851e thermogravimetric analyzer (Mettler-Toledo, Schwerzenbach, Switzerland), where the samples were heated from room temperature to 800 ℃ at a rate of 1 ℃/min.

2.1.6. Rotating Disk Electrode (RDE) Measurements

2 mg sample was dissolved in 0.5 mL ethanol and 10 μL Nafion solution under sonication for 30 min. The working electrode was prepared by applying a drop of the suspension (50 μL) to a disc electrode. The Ag/AgCl electrode and graphite electrode were used as the reference and counter electrodes, respectively. Linear scanning voltammetry (LSV) curves were tested in a 0.1 M Na_2HPO_4/NaH_2PO_4 solution (pH = 7) with a continuous oxygen flow at different rotational speeds. The slope of the n value according to the Koutecky-Levich (K-L) plot was calculated based on the following equation

$$B = 0.62nFCD^{2/3}\nu^{-1/6} \quad (1)$$

$$j^{-1} = j_k^{-1} + B^{-1}\omega^{-1/2} \quad (2)$$

In the aforementioned context, j represents the measured current density, j_k signifies the kinetic current density. ω is the angular rotation rate (rad s^{-1}), converted from the electrode rotation speed N in rpm using $\omega = 2\pi N/60$. F is the Faraday constant (96,485 Coulombs per mole), and C is the bulk concentration of oxygen in water (1.26×10^{-6} mol cm^{-3}). Furthermore, ν denotes the hydrodynamic viscosity of water, which has been measured to be 0.01 cm^2 s^{-1}, while D represents the diffusion coefficient of oxygen, which is 2.7×10^{-5} cm^2 s^{-1}.

2.2. Synthetic Procedures of Covalent Organic PolymersD

Synthesis of PP-COP-**9**

As shown in Figure 1, Tetrakis(4-Aminophenyl)Methane (76 mg, 0.2 mmol), benzaldehyde (84.9 mg, 0.8 mmol) and *p*-Toluenesulfonic acid (28 mg) were added into 2.5 mL acetic acid within a 10 mL Pyrex tube (Beijing Synthware Glass Inc., Beijing, China). The mixture was subjected to sonication and heated at 90 °C for 30 min to conduct a preliminary reaction. After the addition of 34.4 μL of butane-2,3-dione, the reaction was allowed to proceed at 90 °C under air for 72 h. Subsequently, the product was washed three times with acetic acid and pure water, resulting in a black solid. After being purified via Soxhlet extraction with THF for three days, the product was obtained as a brownish-yellow solid in 90% yield.

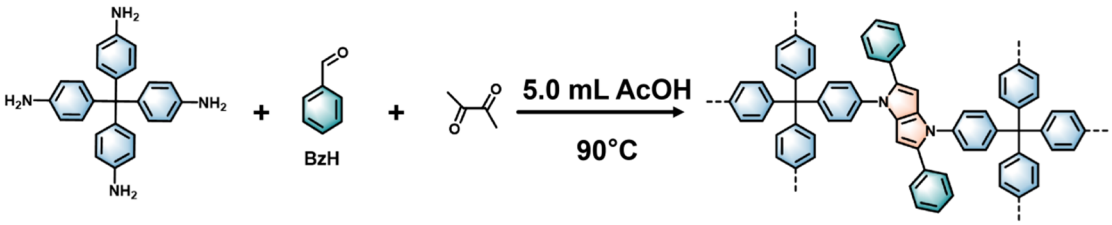


Figure 1. Schematic synthesis of PP-COP-**9**.

2.3. H_2O_2 Photosynthesis Experiment

2.3.1. Batch Photocatalytic H_2O_2 Production

Photocatalyst (3 mg) was dispersed in a photocatalytic reactor containing 30 mL of deionized water. The catalyst was dispersed by sonication for 30 min, during which O_2 was bubbled into the suspension throughout the photocatalytic process. The reaction was conducted using a light-source system (CEL-S500, CeauLight Co., Ltd., Beijing, China) interchangeable monochromatic lamp heads at 365 nm, 420 nm and 550 nm, respectively, as the light source. The concentration of H_2O_2 was determined using a UV-Vis spectrophotometer. During the light irradiation process, 1.0 mL of solution was removed from the photocatalytic reactor and the catalyst particles were removed using a 0.22 μm filter. The concentration of H_2O_2 produced was then detected by iodometric colourimetry

(measured by the absorption peak at approximately 350 nm). In a typical experiment, 1 mL of the sample was filtered through a 0.22 μm Millipore filter (13 mm diameter, TYLQ-0001UC; Shanghai Titan Scientific Co., Ltd., Shanghai, China), transferred to a 10 mL chromatographic tube, and diluted with deionized water to 5 mL. After mixing, 500 μL of $C_8H_5KO_4$ (0.1 mol L^{-1}) and 500 μL of KI (0.4 mol L^{-1}) ($H_2O_2 + 3I^- + 2H^+ \rightarrow I_3^- + 2H_2O$) were added to the sample tube and mixed. Subsequently, the mixture was incubated in the dark for 30 min and analyzed by a UV-2600 spectrometer, with an absorption peak of approximately 350 nm. Throughout the entire process, the resulting H_2O_2 was tested on three separate occasions, with the average value being calculated. The linear relationship between H_2O_2 concentration and absorbance at 350 nm was established using the calibration curve shown in Figure 2B and expressed by Equation (3). The corresponding UV-vis absorption spectra are presented in Figure 2A. (All samples using benzyl alcohol as the sacrificial agent were diluted 50 times for measurement).

$$Y = 250.22A - 7.84 \quad (3)$$

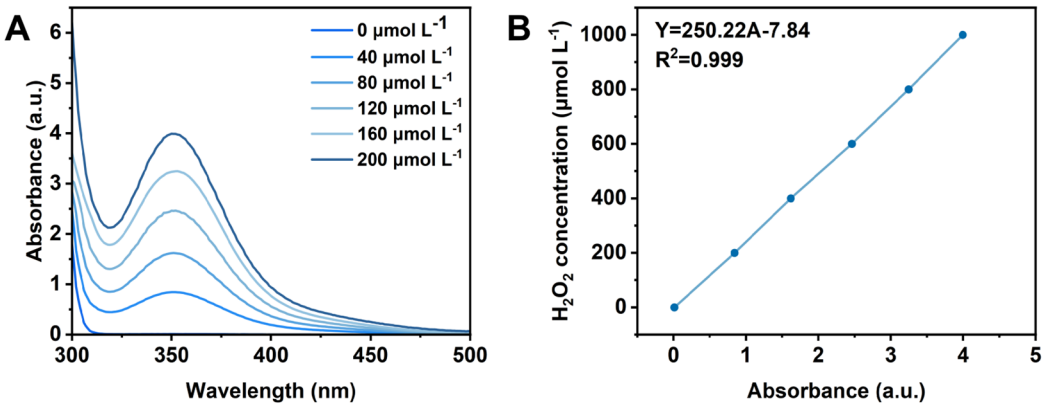


Figure 2. (**A**) UV–vis absorption spectra of H_2O_2 standards after reaction with the iodometric reagents. (**B**) Corresponding calibration curve relating H_2O_2 concentration to absorbance at 350 nm.

2.3.2. Photocatalytic Recycling Experiment

Photocatalytic recovery experiments were conducted using the following methods. To keep the same amount of COPs photocatalyst (3 mg) in each cycle, the COPs sample (approximately 60 mg) was suspended in 30 mL of O_2 saturated water and irradiated for 1 h under visible light (λ > 365 nm). Collect the solid by filtration, wash three times with water and ethanol, and vacuum dry at 60 °C for 12 h. Then, take 3 mg COPs for the second cycle test. The remaining solid was treated again in fresh O_2 saturated water and irradiated for 1 h. After collection, washing, and drying, an additional 3 mg of treated catalyst was used in the third cycle. The above procedure was repeated in the fourth and fifth cycles of testing. The testing conditions are the same as the initial experiment of photocatalytic H_2O_2 production.

3. Results and Discussion

3.1. Synthesis and Characterization

As shown in Figure 3A, PP-COP-**9** was constructed from tetrakis(4-aminophenyl)methane (TAPM), benzaldehyde (BzH), and 2,3-butanedione through an acetic-acid-mediated multicomponent cyclization reaction, during which pyrrolo[3,2-*b*]pyrrole (PP) conjugated units were formed *in situ* and further extended into the polymer network. Frontier molecular orbital analysis was further performed on a representative structural model to elucidate the intrinsic electronic structure of PP-COP-**9** (Figure 3B). The HOMO is mainly localized on the PP conjugated core and adjacent aromatic moieties, whereas the LUMO extends toward the neighboring aromatic segments, exhibiting a spatially differentiated orbital distribution. Such frontier-orbital separation suggests a favorable tendency for photoinduced charge redistribution and migration within the conjugated framework.

As shown in Figure S1, the C=O stretching vibration of the aldehyde monomer at 1674 cm^{-1} nearly disappeared in PP-COP-**9**, accompanied by the emergence of characteristic absorption bands at 1610, 1422, and 1267 cm^{-1}, which were assigned to the pyrrolo[3,2-*b*]pyrrole (PP) structural units. These spectral changes confirm the consumption of aldehyde groups and the formation of PP units during the multicomponent cyclization, supporting the successful construction of the polymer framework. The local chemical structure of PP-COP-**9** was further characterized by ^{13}C cross-polarization magic angle spinning (CP-MAS) solid-state NMR spectroscopy (Figure 4A). The resonance signals in the range of 113.1–144.1 ppm were mainly assigned to the aromatic carbons

(C=C and C-N) within the conjugated framework, among which the signal at 113.1 ppm was attributed to the C-H carbon of the pyrrolyl unit. In addition, the characteristic resonance at 62.5 ppm was assigned to the aliphatic C-C carbon of the TAPM moiety, further confirming the incorporation of the three-dimensional structural unit into the polymer network.

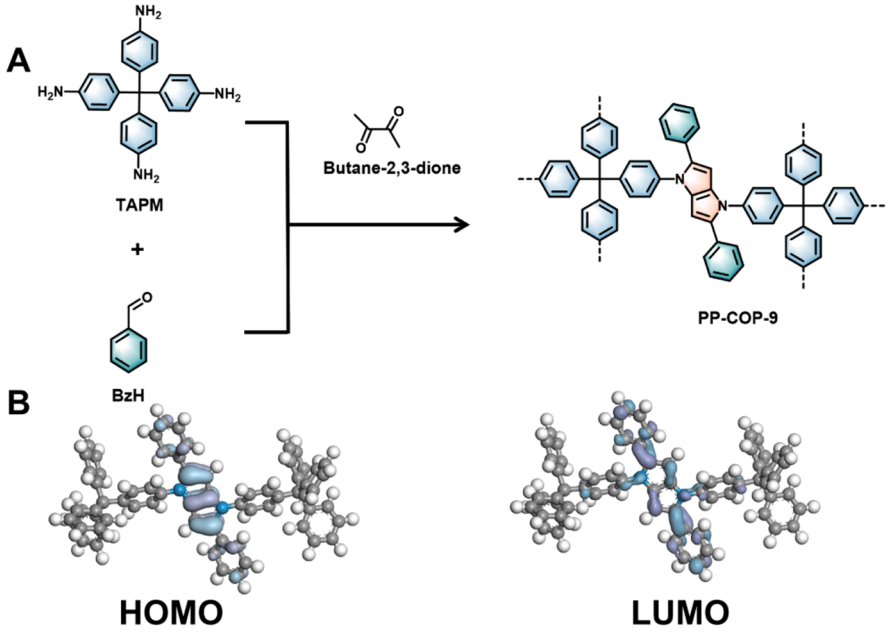


Figure 3. (**A**) Schematic synthesis of PP-COP-**9**. (**B**) HOMO and LUMO distributions of PP-COP-**9**.

X-ray photoelectron spectroscopy (XPS) analysis further provided insight into the chemical environment of nitrogen species within the polymer. The high-resolution N 1s spectrum (Figure 4B) exhibited a characteristic peak at 397.2 eV, which was assigned to the C-N-C nitrogen species in the pyrrolo[3,2-*b*]pyrrole (PP) units, further confirming the formation of the PP-based heterocyclic structure within the polymer framework. Taken together, the consistent spectroscopic results obtained from FT-IR, ^{13}C CP/MAS NMR, and high-resolution XPS collectively supported the successful construction and structural integrity of PP-COP-**9** from the perspectives of functional-group conversion, carbon-framework composition, and the chemical environment of nitrogen species.

Scanning electron microscopy (SEM) images revealed that PP-COP-**9** exhibited a relatively uniform spherical morphology with micrometer-scale particle sizes (Figure S2). Energy-dispersive X-ray spectroscopy (EDS) elemental mapping further revealed a homogeneous distribution of C and N throughout the PP-COP-**9** particles (Figure S3), confirming the elemental uniformity of the polymer framework. In addition, thermogravimetric analysis (TGA) demonstrated the good thermal stability of PP-COP-**9**, with more than 80% of its initial mass retained at 400 °C (Figure S4).

To investigate the influence of the three-dimensional framework configuration on the optoelectronic properties of PP-COP-**9**, its optical characteristics were first examined by ultraviolet-visible diffuse reflectance spectroscopy (UV-vis DRS). As shown in Figure 4C, PP-COP-**9** exhibited broad absorption across both the ultraviolet and visible-light regions. Compared with the corresponding monomers, PP-COP-**9** exhibited a markedly extended absorption edge after polymerization, indicating enhanced electronic delocalization and altered electronic structure within the extended polymer framework. The three-dimensional and non-coplanar framework, together with the electron-rich pyrrolo[3,2-*b*]pyrrole units, provides a distinct spatial electronic coupling environment within the conjugated network. The optical band gap (E_g) of PP-COP-**9** was determined to be 2.26 eV from the Tauc plot (Figure 4C), indicating its favorable capability for visible-light utilization. Mott-Schottky analysis was further performed to determine the band structure of PP-COP-**9**, revealing a conduction band (CB) potential of −0.72 V versus the normal hydrogen electrode (NHE) (Figure 4D). Based on the optical band gap, the valence band (VB) potential was calculated to be approximately 1.54 V (vs. NHE, Figure 4E), which was consistent with the result obtained from valence-band X-ray photoelectron spectroscopy (VB-XPS) (Figure S5). These results demonstrate that PP-COP-**9** possesses broad light absorption and suitable band-edge positions, while its negative CB potential provides a favorable thermodynamic basis for photogenerated-electron-driven O_2 reduction. Thus, the interplay between

three-dimensional framework configuration and electronic structure establishes a favorable energetic basis for O_2 activation and subsequent photocatalytic H_2O_2 production.

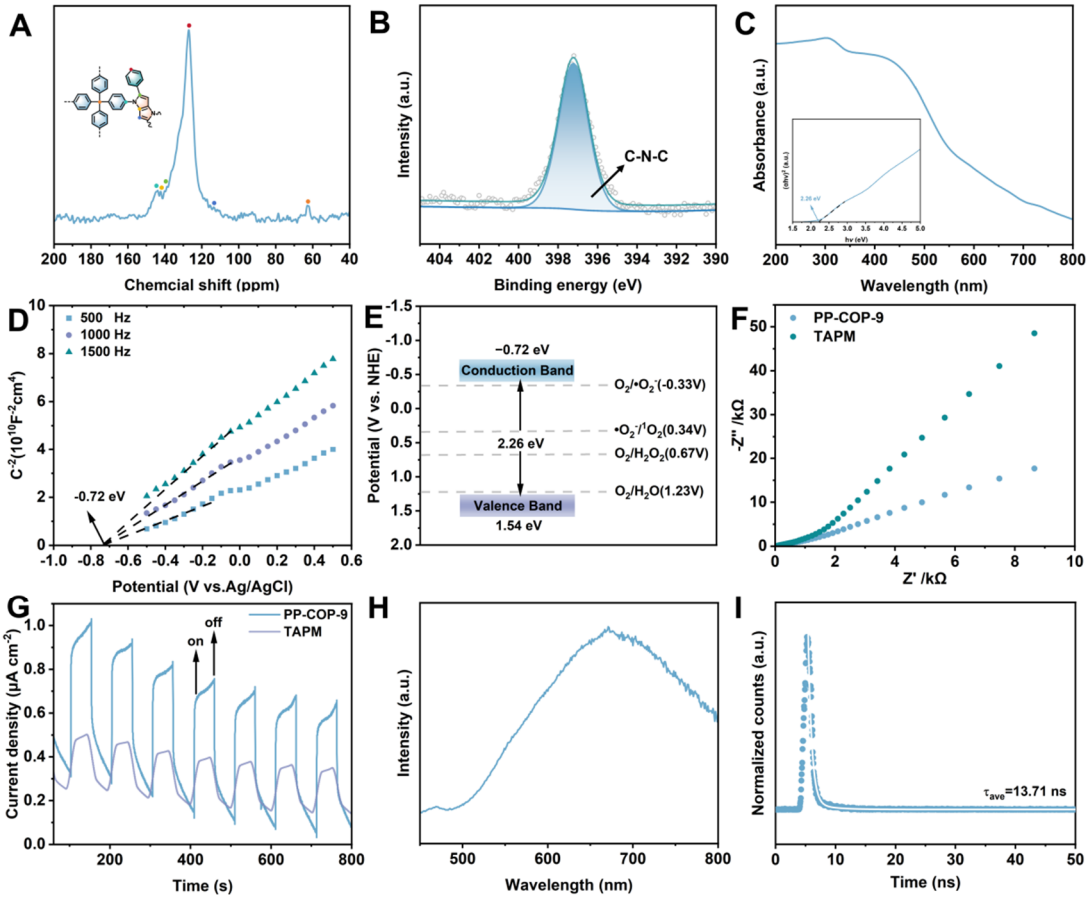


Figure 4. (**A**) ^{13}C NMR spectra of PP-COP-**9**. (**B**) N 1s XPS analysis of PP-COP-**9**. (**C**) UV-vis spectra and band gap characterization of PP-COP-**9**. (**D**) Mott-Schottky plots of PP-COP-**9**. (**E**) Schematic diagram of the band structure of PP-COP-**9**. (**F**) EIS characterization of PP-COP-**9** and TAPM. (**G**) Transient photocurrent responses of PP-COP-**9** and TAPM. (**H**) Steady-state PL spectra of PP-COP-**9**. (**I**) Time-resolved photoluminescence decay curves of PP-COP-**9**.

The photogenerated charge dynamics of PP-COP-**9** were further investigated by transient photocurrent response, electrochemical impedance spectroscopy (EIS), and steady-state photoluminescence (PL) measurements. As shown in Figure 4F, PP-COP-**9** exhibited a lower charge-transfer resistance than the corresponding precursors, indicating that the formation of the polymer framework effectively facilitated interfacial charge transfer and photogenerated carrier migration. Meanwhile, PP-COP-**9** displayed a markedly enhanced transient photocurrent response (Figure 4G), further demonstrating its more efficient separation and transport of photogenerated charge carriers. Photoluminescence measurements further revealed the distinct excited-state dynamics of PP-COP-**9**. Under excitation at 365 nm, PP-COP-**9** exhibited a distinct fluorescence emission centered at approximately 660 nm (Figure 4H). PL measurements revealed an average fluorescence lifetime of 13.71 ns (Figure 4I), indicating the presence of long-lived photoexcited states in PP-COP-**9**. Combined with the enhanced photocurrent response and reduced charge-transfer resistance, these results suggested that the three-dimensional nonplanar framework did not simply compromise charge transport, but instead modulated the spatial arrangement and electronic coupling between conjugated units, thereby preserving efficient charge migration while prolonging the lifetime of the photoexcited states. The resulting long-lived photoexcited states provided an extended time window for photogenerated electrons to migrate toward the catalytic interface and participate in subsequent O_2 activation, thereby creating favorable kinetic conditions for photocatalytic H_2O_2 production via oxygen reduction.

3.2. H_2O_2 Photosynthesis

Based on the favorable light-harvesting capability, band structure, and photogenerated charge dynamics of PP-COP-**9**, its photocatalytic performance for H_2O_2 production was further evaluated. The interfacial wettability

of PP-COP-**9** was first examined by static contact-angle measurements. As shown in Figure S6, PP-COP-**9** exhibited a water contact angle of approximately 120°, indicating its pronounced hydrophobic character. As the H_2O_2 concentration increased from 1% to 10%, the contact angle gradually increased, indicating distinct interfacial interactions of PP-COP-**9** with H_2O and H_2O_2. The change in contact angle indicates different wetting behavior of PP-COP-**9** in H_2O_2-containing aqueous media; however, contact-angle measurements alone do not directly establish H_2O_2 desorption from the catalytic surface. The stability of H_2O_2 in the presence of PP-COP-**9** was further evaluated through photodecomposition experiments. As shown in Figure S7, more than 85% of the initial H_2O_2 remained after 8 h of continuous irradiation, indicating that relatively low catalytic decomposition activity of PP-COP-**9** toward H_2O_2. The low H_2O_2 decomposition activity of PP-COP-**9** helps minimize secondary product consumption, thereby promoting sustained H_2O_2 accumulation.

Subsequently, the photocatalytic H_2O_2 production performance of PP-COP-**9** was evaluated under irradiation from a 300 W Xe lamp, and the generated H_2O_2 was quantified using the iodometric method [38–43]. Under dark conditions, a low H_2O_2 production rate of 146 μmol g^{-1} h^{-1} was observed, which was approximately 2.8% of that obtained under irradiation (5269 μmol g^{-1} h^{-1}), confirming that the high H_2O_2 production activity is predominantly photo-driven (Figure S8). Wavelength-dependent experiments further showed that the H_2O_2 production activity followed the photoresponse of PP-COP-**9**, reaching a maximum rate of 5269 μmol g^{-1} h^{-1} under 365 nm monochromatic irradiation. H_2O_2 production was markedly suppressed under N_2 or Ar but significantly enhanced under O_2, confirming the essential role of molecular oxygen and supporting an oxygen reduction reaction (ORR) pathway for H_2O_2 formation (Figure 5A).

To further improve photogenerated charge utilization, the effects of different hole scavengers on photocatalytic H_2O_2 production were investigated (Figure 5B). The addition of 10% (v/v) methanol, ethanol, or isopropanol resulted in only a slight enhancement in H_2O_2 production, whereas the introduction of 10% (v/v) benzyl alcohol (BA) dramatically increased the H_2O_2 production rate to 118,936 μmol g^{-1} h^{-1}, approximately 23 times that obtained in pure water. Such a remarkable enhancement can be attributed to efficient hole scavenging by BA together with the favorable interfacial environment established in the BA/H_2O biphasic system [44–47]. The hydrophobic PP-COP-**9** was expected to preferentially reside in the organic phase or at the biphasic interface, whereas the generated H_2O_2 predominantly partitioned into the aqueous phase, thereby reducing its prolonged contact with the photocatalyst and suppressing secondary decomposition. Thus, efficient hole scavenging and biphasic product separation synergistically promote both H_2O_2 formation and accumulation.

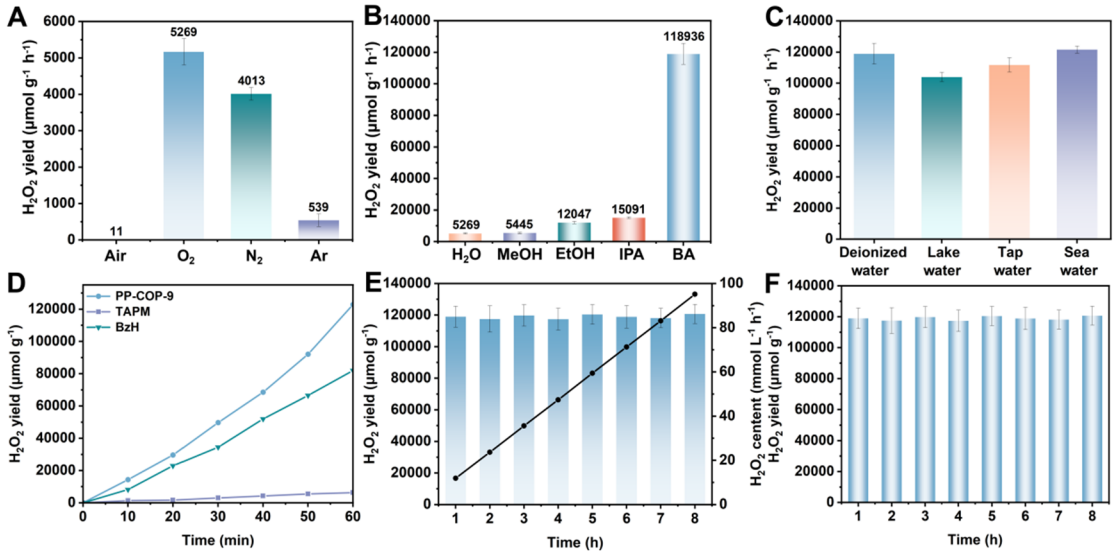


Figure 5. (**A**) Photocatalytic H_2O_2 production under different atmospheres. (**B**) Schematic representation of H_2O_2 yields of PP-COP-**9** in different sacrificial agents. (**C**) Photocatalytic H_2O_2 production performance for PP-COP-**9** in different water matrices. (**D**) Schematic representation of H_2O_2 yields of PP-COP-**9**, TAPM, and BzH in a 10% benzyl alcohol system. (**E**) Yield of H_2O_2 produced by PP-COP-**9** over 8 h in continuous reaction. (**F**) Recycle results for PP-COP-**9** catalyzed H_2O_2 production.

Given the high H_2O_2 production activity of PP-COP-**9** in the BA-assisted system, its performance in complex water matrices was further evaluated. Photocatalytic tests were conducted using deionized water, tap water, lake water, and artificial seawater as the aqueous phases (Figure 5C). The activity in tap water was only slightly lower than that in deionized water, while an H_2O_2 production rate of approximately 100,000 μmol g^{-1} h^{-1} was still

achieved in the more compositionally complex lake water, indicating good tolerance toward common coexisting species. Notably, the H_2O_2 production rate observed in artificial seawater was even higher than that in deionized water, demonstrating the good tolerance of PP-COP-**9** toward high-ionic-strength environments.

To clarify the contribution of polymer framework construction to the photocatalytic performance, the H_2O_2 production activities of the corresponding precursors were further evaluated under identical conditions (Figure 5D). All precursors exhibited substantially lower activities than PP-COP-**9**, indicating that the enhanced H_2O_2 photosynthesis originates from the integrated polymer framework rather than from the individual chromophoric units alone. Combined with the spectroscopic, photoelectrochemical, and excited-state dynamics results, these findings suggest that the three-dimensional nonplanar framework promotes favorable charge separation and interfacial charge transfer, thereby facilitating subsequent interfacial O_2 activation. In addition to its high H_2O_2 production activity, PP-COP-**9** also exhibited good photocatalytic durability. During 8 h of continuous irradiation, PP-COP-**9** maintained stable H_2O_2 production performance (Figure 5E). After five consecutive photocatalytic cycles, PP-COP-**9** still retained high photocatalytic activity (Figure 5F), while no noticeable changes were observed in the FTIR spectrum of the recovered catalyst (Figure S9), demonstrating its good photocatalytic durability and structural stability.

Electron paramagnetic resonance (EPR) spectroscopy was further employed to elucidate the H_2O_2 formation pathway [48–53]. As shown in Figure 6A,B, distinct DMPO-$\cdot O_2^-$ characteristic signals were observed upon light irradiation, together with the detection of $^1O_2$, demonstrating the effective activation of molecular oxygen by PP-COP-**9**. The formation of $\cdot O_2^-$ was consistent with the aforementioned O_2-dependent experiments, supporting the transfer of photogenerated electrons to O_2 to form $\cdot O_2^-$ intermediates, followed by subsequent proton-coupled electron-transfer steps toward H_2O_2 formation. These results suggest that H_2O_2 formation over PP-COP-**9** predominantly follows a $\cdot O_2^-$-mediated stepwise ORR pathway, while $^1O_2$ likely originates from a parallel O_2 activation process.

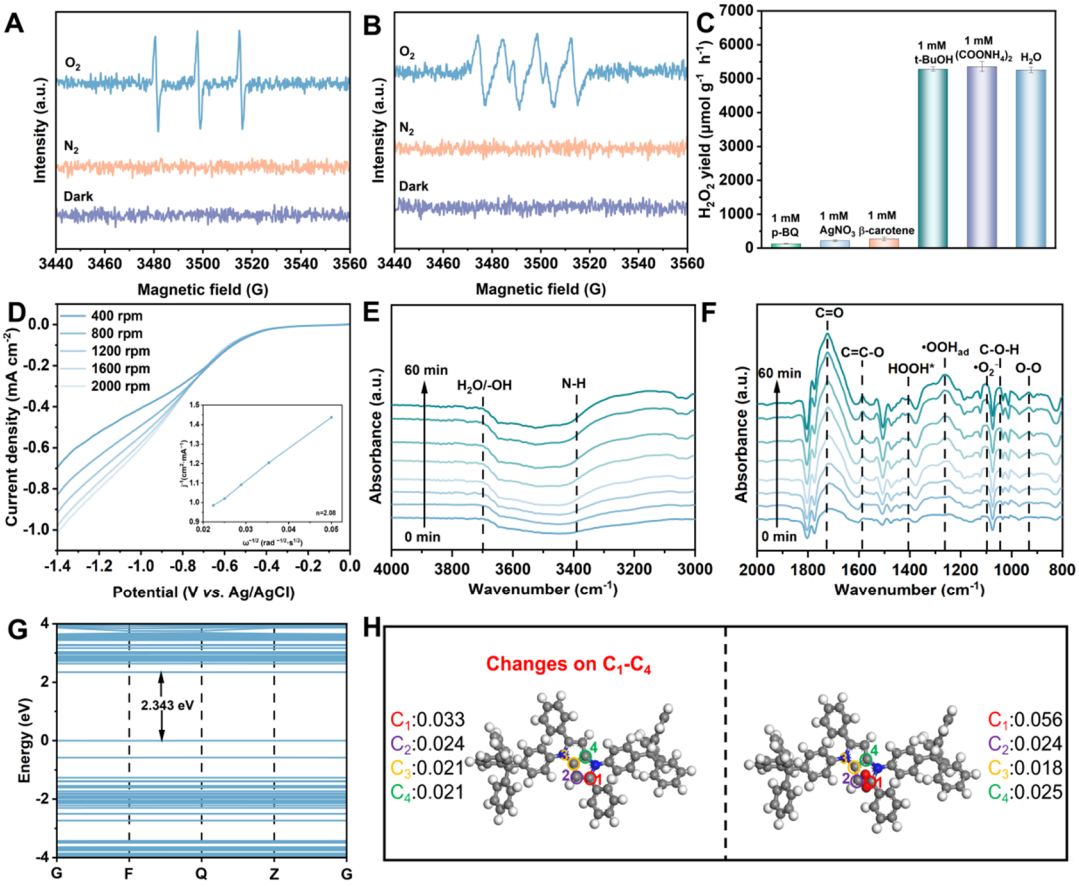


Figure 6. (**A**) PP-COP-**9** under dark, O_2 and N_2 conditions using DMPO as spin-trapping agents. (**B**) PP-COP-**9** under dark, O_2 and N_2 conditions using TEMP as spin-trapping agents. (**C**) H_2O_2 production rates of PP-COP-**9** with different photoactive species scavengers. (**D**) Linear-sweep RDE voltammograms of PP-COP-**9** at various rotating speeds. (**E**,**F**) *In Situ* FTIR spectra of PP-COP-**9** during the photocatalytic H_2O_2 evolution process. (**G**) Calculated band structures of PP-COP-**9**. (**H**) Mulliken charge variations at the C_1–C_4 sites of PP-COP-**9** before and after adsorption.

The two-electron oxygen reduction reaction (2e⁻ ORR) for photocatalytic H_2O_2 production can proceed through either a $\cdot O_2^-$-mediated stepwise single-electron transfer pathway or a direct two-electron transfer pathway. To elucidate the ORR pathway over PP-COP-**9**, reactive-species trapping experiments and rotating disk electrode (RDE) measurements were further performed. As shown in Figure 6C, *p*-BQ and *β*-carotene markedly suppressed H_2O_2 production, indicating the involvement of $\cdot O_2^-$ and $^1O_2$ in O_2 activation, whereas 0.1 M *t*-BuOH caused only an approximately 2% decrease, suggesting a negligible contribution from ·OH. The addition of 0.1 mM $AgNO_3$ substantially suppressed H_2O_2 production, confirming the key role of photogenerated electrons in the ORR, whereas ammonium oxalate slightly enhanced H_2O_2 production by consuming photogenerated holes. Koutecky-Levich (K-L) analysis yielded an average electron-transfer number of 2.08, close to the theoretical value of 2, confirming a predominant two-electron ORR pathway (Figure 6D). Combined with the EPR and trapping results, these findings support a $\cdot O_2^-$-mediated stepwise pathway for H_2O_2 formation, while $^1O_2$ likely participates in a parallel O_2 activation process.

In-Situ diffuse reflectance infrared Fourier transform spectroscopy (DRIFTS) was further employed to monitor the evolution of key intermediates during photocatalysis. As shown in Figure 6E,F, upon prolonged irradiation, characteristic bands assigned to HOOH* and adsorbed ·OOH species emerged at approximately 1400 and 1250–1300 cm^{-1}, respectively, while signals related to $\cdot O_2^-$ and O-O vibrations appeared at 1050–1100 and 900 cm^{-1}. The sequential evolution of these intermediates supports a $\cdot O_2^-$-mediated two-electron ORR pathway toward H_2O_2 formation. Moreover, the C=C-O-related features at 1580–1600 cm^{-1} and the C=O-related feature at ca. 1700 cm^{-1} are consistent with the evolution of oxygen-containing surface species under illumination. Since their exact structures and adsorption sites cannot be unambiguously established from DRIFTS alone, these bands are not used to assign a specific active site for interfacial O_2 activation.

To further elucidate the electronic origin of the 2e⁻ ORR activity, DFT calculations were performed. The calculated band structure of PP-COP-**9** exhibits a band gap of 2.343 eV, in good agreement with the experimental value of 2.26 eV, confirming its semiconducting nature (Figure 6G). DOS analysis further reveals that the electronic states near the band edges are predominantly contributed by carbon-derived orbitals, indicating that the carbon framework plays an important role in interfacial electron transfer (Figure S10). Consistently, *OOH adsorption induces pronounced Mulliken charge redistribution at the C_1–C_4 sites, with C_1 exhibiting the largest variation from 0.033 to 0.056 (Figure 6H). This pronounced electronic response, together with the carbon-dominated frontier states, identifies C_1 as a potential active site for *OOH interaction and activation during the 2e⁻ ORR. These theoretical results complement the DRIFTS observations and provide an electronic-level rationale for the formation and stabilization of key oxygenated intermediates on PP-COP-**9**.

To further evaluate the continuous H_2O_2 production capability of PP-COP-**9**, a spiral-coil continuous-flow photoreactor was constructed (Figure 7A), and the effects of the gas-to-liquid flow-rate ratio (V_g/V_L) was systematically investigated (Figure 7B). At $V_g/V_L = 2$, the H_2O_2 concentration reached a maximum of 21.42 mM after 60 min, approximately 1.8 times that obtained in the conventional batch reactor, suggesting that the continuous-flow configuration promotes O_2 supply and interfacial mass transfer. Under the optimized conditions ($V_g/V_L = 2$, 10% BA), the system enabled stable and continuous H_2O_2 production (Figure 7C). During 8 h of continuous operation, the H_2O_2 concentration was maintained at approximately 21.36 mM, demonstrating robust continuous-production capability. Compared with previously reported polymer-based photocatalytic systems, the PP-COP-**9** continuous-flow system exhibited competitive H_2O_2 production performance (Figure 7D and Table S1). These results demonstrated that coupling PP-COP-**9** with a continuous-flow photoreaction enables efficient and stable H_2O_2 production, highlighting its potential for continuous solar-driven H_2O_2 synthesis.

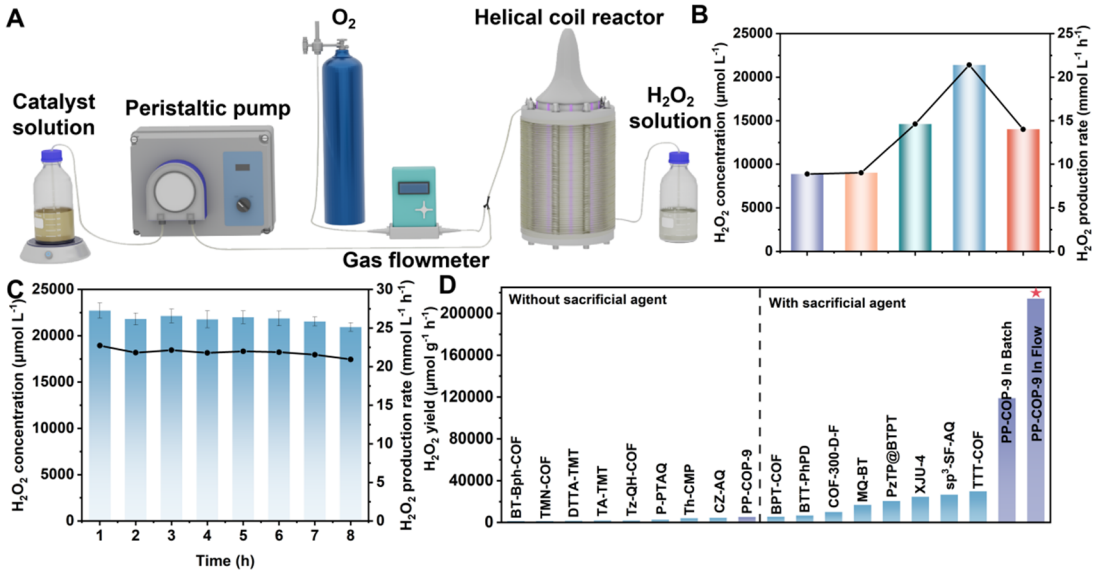


Figure 7. (**A**) Schematic representation of the spiral coil photoreactor system and the photocatalytic H_2O_2 synthesis process. (**B**) Schematic representation of H_2O_2 yield at different gas-liquid ratio. (**C**) Schematic diagram of the yield of PP-COP-**9** during a continuous 8-h reaction. (**D**) Comparison of the H_2O_2 yield for PP-COP-**9** with the reported representative metal-free photocatalysts.

4. Conclusions

In summary, three-dimensional pyrrolo[3,2-*b*]pyrrole-based covalent organic polymers were constructed, revealing the important role of framework spatial configuration regulation in photocatalytic H_2O_2 production. The optimized PP-COP-**9** exhibited favorable light harvesting, suitable band-edge positions, and efficient photogenerated charge dynamics, while its prolonged excited-state lifetime facilitated interfacial electron transfer and O_2 activation. In pure water, PP-COP-**9** achieved an H_2O_2 production rate of 5269 μmol g^{-1} h^{-1}; upon the addition of 10% BA, the production rate was markedly increased to 118,936 μmol g^{-1} h^{-1} through the synergistic effects of efficient hole scavenging and the biphasic interfacial environment. Atmosphere-controlled experiments, EPR measurements, and reactive-species trapping tests further supported the critical role of O_2 reduction in H_2O_2 formation, with $\cdot O_2^-$ identified as a key reaction intermediate and ·OH making a negligible contribution.

In addition to its high activity, PP-COP-**9** exhibited low H_2O_2 decomposition activity, good cycling stability, and excellent tolerance toward complex water matrices. Upon integration into a spiral-coil continuous-flow photoreactor, stable H_2O_2 production at approximately 21.36 mM was maintained for 8 h under optimized conditions. These results establish a structure-function relationship linking the three-dimensional framework configuration, excited-state charge dynamics, O_2 activation, and H_2O_2 production, and further demonstrate the effectiveness of integrating molecular-level framework engineering with continuous-flow reaction design for efficient and stable H_2O_2 photosynthesis.

Supplementary Materials

The additional data and information can be downloaded at: https://media.sciltp.com/articles/others/26111917 11192532/NENP-26090047-SI.pdf. Figure S1: FT-IR spectra of as-prepared PP-COP-**9**, TAPM and BzH. Figure S2: Scanning electron microscopy images (SEM) of PP-COP-**9**. Figure S3: EDS mapping of PP-COP-**9**. Figure S4: TGA curves of PP-COP-**9** under a N_2 atmosphere. Figure S5: XPS valence band spectra of PP-COP-**9**. Figure S6: Water contact angle measurements of PP-COP-**9**. Figure S7: Photocatalytic H_2O_2 decomposition experiments in water with an initial H_2O_2 concentration of 1 mM. Figure S8: Wavelength-dependent H_2O_2 yield rates for PP-COP-**9**. (Test conditions: 3 mg photocatalyst, 30 mL of pure water, O_2 atmosphere, 300 W Xe lamp). Figure S9: FTIR spectra of PP-COP-**9** before and after the photocatalytic reaction. Figure S10: Density of states (DOS) analysis of PP-COP-**9**. Table S1: The performance of PP-COPs in photocatalytic production of H_2O_2, as compared to the most advanced photocatalysts reported to date. The references [54–60] are cited in the Supplementary Materials.

Author Contributions

X.Y.: Methodology, data curation, formal analysis; H.C.: Data curation, formal analysis; S.W.: Methodology; Y.L.: Conceptualization, supervision, writing—original draft preparation, writing—reviewing and editing; D.J.:

Validation; X.C.: Validation; C.Y.: Conceptualization, writing—reviewing and editing. All authors have read and agreed to the published version of the manuscript.

Funding

This work was financially supported by the National Natural Science Foundation of China (22301111) and the China Postdoctoral Science Foundation (2024M751226).

Data Availability Statement

Data are contained within the article.

Conflicts of Interest

The authors declare no conflict of interest.

Use of AI and AI-Assisted Technologies

No AI tools were utilized for this paper.

References

1. Liang, Y.; Wei, J.; Qiu, X.; et al. Homogeneous Oxygenase Catalysis. *Chem. Rev.* **2018**, *118*, 4912–4945. https://doi.org/10.1021/acs.chemrev.7b00193.
2. Zhao, W.; Yan, P.; Li, B.; et al. Accelerated Synthesis and Discovery of Covalent Organic Framework Photocatalysts for Hydrogen Peroxide Production. *J. Am. Chem. Soc.* **2022**, *144*, 9902–9909. https://doi.org/10.1021/jacs.2c02666.
3. Subramanian, G.; Prakash, H. Photo Augmented Copper-based Fenton Disinfection under Visible LED Light and Natural Sunlight Irradiation. *Water Res.* **2021**, *190*, 116719. https://doi.org/10.1016/j.watres.2020.116719.
4. Yamanaka, I.; Murayama, T. Neutral H_2O_2 Synthesis by Electrolysis of Water and O_2. *Angew. Chem. Int. Ed.* **2008**, *47*, 1900–1902. https://doi.org/10.1002/anie.200704431.
5. Zhi, Q.; Liu, W.; Jiang, R.; et al. Piperazine-Linked Metalphthalocyanine Frameworks for Highly Efficient Visible-Light-Driven H_2O_2 Photosynthesis. *J. Am. Chem. Soc.* **2022**, *144*, 21328–21336. https://doi.org/10.1021/jacs.2c09482.
6. Yuan, Y.; Chen, L.; Wan, Z.; et al. Electrocatalytic ORR–coupled ammoximation for efficient oxime synthesis. *Sci. Adv.* **2024**, *10*, eado1755. https://doi.org/10.1126/sciadv.ado1755.
7. Yu, H.; Zhang, F.; Chen, Q.; et al. Vinyl-Group-Anchored Covalent Organic Framework for Promoting the Photocatalytic Generation of Hydrogen Peroxide. *Angew. Chem. Int. Ed.* **2024**, *63*, e202402297. https://doi.org/10.1002/anie.202402297.
8. Burek, B.O.; Bormann, S.; Hollmann, F.; et al. Hydrogen peroxide driven biocatalysis. *Green Chem.* **2019**, *21*, 3232–3249. https://doi.org/10.1039/c9gc00633h.
9. Fadaee, M.M.; Doyle, B.J.; Roberge, D.M.; et al. Liquid flow field and residence time distribution in a baffleless oscillatory flow coil reactor. *Chem. Eng. J.* **2024**, *492*, 151758. https://doi.org/10.1016/j.cej.2024.151758.
10. Ma, H.; Zhang, Y.; Wu, Y.; et al. Regulation of charge carrier transportation in D–π–A type covalent organic frameworks for promoting photocatalytic H_2O_2 production. *Chem. Sci.* **2025**, *16*, 16668–16677. https://doi.org/10.1039/d5sc02875b.
11. Wang, W.; Wang, L.; Sun, L.; et al. Se–Se bonds induced highly metallic 1T' $MoSe_{2.3}$ nanosheets cocatalysts towards boosted H_2O_2 photosynthesis over NH_2-MIL-125 derived TiO_2 nanotablets. *Chem. Eng. J.* **2023**, *477*, 146945. https://doi.org/10.1016/j.cej.2023.146945.
12. Chai, X.; Gao, R.T.; Wang, L. Electron transport kinetics via ZnO with ultralow Fe dopant for stable oxygen reduction to H_2O_2. *Chem. Eng. J.* **2024**, *484*, 149527. https://doi.org/10.1016/j.cej.2024.149527.
13. Jing, S.; Zhao, J.; Wang, A.; et al. Efficient photocatalytic production of H_2O_2 and photodegradation of tetracycline by CdS/square tubular g-C_3N_4 S-scheme heterojunction photocatalyst. *Chem. Eng. J.* **2024**, *479*, 147150. https://doi.org/10.1016/j.cej.2023.147150.
14. Zhang, Q.; Wang, B.; Miao, H.; et al. Efficient photocatalytic H_2O_2 production over K^+-intercalated crystalline g-C_3N_4 with regulated oxygen reduction pathway. *Chem. Eng. J.* **2024**, *482*, 148844. https://doi.org/10.1016/j.cej.2024.148844.
15. Sun, C.; Shi, Y.; Unno, M.; et al. Hydrogen-Bond Engineered Porphyrin-Polyimide Aerogels for Sustainable Photocatalytic H_2O_2 Production from Water and O_2. *ACS Sustain. Chem. Eng.* **2025**, *13*, 17422–17435. https://doi.org/10.1021/acssuschemeng.5c07062.
16. Zhang, Y.; Lewis, R.J.; Li, Z.; et al. Direct Synthesis of H_2O_2 by Spatially Separate Hydrogen and Oxygen Activation Sites on Tailored Pt–Au Catalysts. *Angew. Chem. Int. Ed.* **2026**, *65*, e21118. https://doi.org/10.1002/anie.202521118.
17. Kim, C.; Park, S.O.; Kwak, S.K.; et al. Concurrent oxygen reduction and water oxidation at high ionic strength for scalable electrosynthesis of hydrogen peroxide. *Nat. Commun.* **2023**, *14*, 5822. https://doi.org/10.1038/s41467-023-41397-1.

18. Liu, R.; Chen, Y.; Yu, H.; et al. Linkage-engineered donor–acceptor covalent organic frameworks for optimal photosynthesis of hydrogen peroxide from water and air. *Nat. Catal.* **2024**, *7*, 195–206. https://doi.org/10.1038/s41929-023-01102-3.
19. Kim, H.W.; Ross, M.B.; Kornienko, N.; et al. Efficient hydrogen peroxide generation using reduced graphene oxide-based oxygen reduction electrocatalysts. *Nat. Catal.* **2018**, *1*, 282–290. https://doi.org/10.1038/s41929-018-0044-2.
20. Liu, Z.L.; Zhou, J.L.; Yuan, S.X.; et al. Asymmetry-Engineered g-C_3N_4 Nanosheets with Dual Electronic-Adsorption Modulation for High-Efficiency Solar-Driven H_2O_2 Synthesis. *Adv. Funct. Mater.* **2026**, *36*, e23126. https://doi.org/10.1002/adfm.202523126.
21. Freese, T.; Meijer, J.T.; Feringa, B.L.; et al. An organic perspective on photocatalytic production of hydrogen peroxide. *Nat. Catal.* **2023**, *6*, 553–558. https://doi.org/10.1038/s41929-023-00980-x.
22. Li, Y.; Chen, H.; Li, Z.; et al. Porous Functional Nanomaterials for Continuous Flow Catalysis. *Nano-Micro Lett.* **2026**, *18*, 300. https://doi.org/10.1007/s40820-026-02149-0.
23. Choi, J.Y.; Check, B.; Fang, X.; et al. Photocatalytic Hydrogen Peroxide Production through Functionalized Semiconductive Metal-Organic Frameworks. *J. Am. Chem. Soc.* **2024**, *146*, 11319–11327. https://doi.org/10.1021/jacs.4c00681.
24. Dong, T.; Xu, X.; Chen, L.; et al. Defective three-dimensional covalent organic frameworks for enhanced hydrogen peroxide photosynthesis and organic transformation. *Nat. Commun.* **2026**, *17*, 4505. https://doi.org/10.1038/s41467-026-71137-0.
25. Huang, P.; Peng, Y.Y.; Wang, X.H.; et al. Charge-Distribution and Microenvironment Dual Regulation of Covalent Organic Frameworks for Enhancing Photocatalytic H_2O_2 and H_2 Production. *Adv. Mater.* **2026**, *38*, e07849. https://doi.org/10.1002/adma.202507849.
26. Luan, T.X.; Wei, Q.; Xin, C.; et al. Remarkably Enhancing H_2O_2 Photogeneration by Modulating Pore-Microenvironment of a Photoactive Covalent Organic Framework. *Adv. Mater.* **2026**, *38*, e15517. https://doi.org/10.1002/adma.202515517.
27. Qin, L.; Yan, Y.; Wu, L.; et al. Spatial Confinement of Photogenerated Electrons at Catalytic Sites in Covalent Organic Frameworks for Efficient Photocatalytic H_2O_2 Production. *Adv. Mater.* **2026**, *38*, e73490. https://doi.org/10.1002/adma.73490.
28. Nan, Q.; Ning, J.; Han, B.; et al. Boosting the photocatalytic H_2O_2 production of covalent organic frameworks with a heteroatom-locked acceptor and gas diffusion system. *Chem. Sci.* **2026**, *17*, 466–474. https://doi.org/10.1039/d5sc05346c.
29. Zhu, S.; He, X.; Wang, L.; et al. Structural Dissimilation of Spirobifluorene-Based Conjugated Microporous Polymers for Efficient Overall Photoproduction of Hydrogen Peroxide. *Adv. Funct. Mater.* **2026**, *36*, e19832. https://doi.org/10.1002/adfm.202519832.
30. Zhang, J.; Zhou, W.; Zhu, C.; et al. Regulating Built-in Electric Fields in Methylquinoline-Derived Vinylene-Linked Covalent Organic Frameworks for Enhanced Photocatalytic H_2O_2 Production. *Angew. Chem. Int. Ed.* **2026**, *65*, e24596. https://doi.org/10.1002/anie.202524596.
31. Fu, M.; He, J.; Li, Y.; et al. Engineering Separated Dual O_2 Reduction Cores into One Polymer Framework for Boosting Hydrogen Peroxide Production. *Adv. Sci.* **2025**, *12*, e08553. https://doi.org/10.1002/advs.202508553.
32. Li, Y.; He, J.; Wang, C.; et al. Construction of pyrrolo[3,2-*b*]pyrrolyl-linked covalent organic polymers to promote continuous overall H_2O_2 production. *Nano Energy* **2024**, *132*, 110397. https://doi.org/10.1016/j.nanoen.2024.110397.
33. Lan, W.; Liu, Q.; Jin, Y.; et al. Beyond Planar Architectures: Oxacalix[4]Arene-Bridged 3D Covalent Organic Frameworks with Saddle-Shaped π-Cavities for Efficient Hydrogen Peroxide Photogeneration and Non-Covalent C60 Confinement. *Small* **2025**, *21*, e07026. https://doi.org/10.1002/smll.202507026.
34. Han, Y.; Huang, C.; Jin, Y.; et al. Enhanced photocatalytic H_2O_2 production via benzyl alcohol−boosted D−π−A covalent organic frameworks in industrial wastewater. *Appl. Catal. B Environ. Energy* **2026**, *395*, 126896. https://doi.org/10.1016/j.apcatb.2026.126896.
35. Sun, T.; Wang, R.; Guan, R.; et al. Design strategies and application progress of covalent organic frameworks in photocatalytic oxidation reactions. *Chem. Sci.* **2026**, *17*, 1964–2000. https://doi.org/10.1039/d5sc08410e.
36. Zheng, Y.; You, S.; Li, S.; et al. All-Conjugated Microporous Polymer Heterojunction with Hierarchical Hollow Sphere Architecture for Photocatalytic H_2O_2 Production. *Adv. Funct. Mater.* **2026**, *36*, e08538. https://doi.org/10.1002/adfm.202508538.
37. Yang, K.; Chen, L.; Xiong, K.; et al. Bisite Sulfonate-Functionalized Covalent Organic Frameworks with Efficient and Dynamic Proton Transportation for Accelerating H_2O_2 Photosynthesis. *Adv. Funct. Mater.* **2026**, *36*, e20900. https://doi.org/10.1002/adfm.202520900.
38. Long, Z.; Luo, K.; Wang, K.; et al. Covalent Organic Cage-Based Photocatalysts for Highly Efficient and Selective H_2O_2 Production. *Adv. Mater.* **2026**, *38*, e20264. https://doi.org/10.1002/adma.202520264.
39. Xie, Z.; Chen, X.; Wang, W.; et al. Variation of Chemical Microenvironment of Pores in Hydrazone-Linked Covalent Organic Frameworks for Photosynthesis of H_2O_2. *Angew. Chem. Int. Ed.* **2024**, *63*, e202410179. https://doi.org/10.1002/anie.202410179.
40. Feng, J.; Wei, Y.; Li, X.; et al. 3D-Printed COF/Zeolite Composites for Augmented Photocatalytic Hydrogen Peroxide Production. *Angew. Chem. Int. Ed.* **2025**, *64*, e202508226. https://doi.org/10.1002/anie.202508226.

41. Gao, J.; Yin, C.; Tang, C.; et al. Ordered Ionic Nanochannels in Covalent Organic Frameworks for Photosynthesis of H_2O_2 From Ambient Air-Equilibrated Water. *Angew. Chem. Int. Ed.* **2026**, *65*, e7617241. https://doi.org/10.1002/anie.7617241.
42. Zdražil, L.; Cadranel, A.; Zoppellaro, G.; et al. Enzyme-inspired single-atom photocatalysis for oxygen reduction to hydrogen peroxide. *Nat. Commun.* **2025**, *16*, 10949. https://doi.org/10.1038/s41467-025-67189-3.
43. Zhu, X.; Chen, L.; Xiong, K.; et al. Extending Asymmetric π-Conjugation of Vinylene-Linked Covalent Organic Frameworks with Remodeled Redox Active Sites for H_2O_2 Photosynthesis and Aerobic Oxidations. *J. Am. Chem. Soc.* **2026**, *148*, 15099–15113. https://doi.org/10.1021/jacs.6c00731.
44. Hu, S.Z.; Yue, M.N.; Liu, Y.; et al. Heterocycle-Linked Covalent Organic Frameworks with Indazole Units for Cooperative H_2O_2 Photosynthesis and Biomass Valorization. *Angew. Chem. Int. Ed.* **2026**, *65*, e8182546. https://doi.org/10.1002/anie.8182546.
45. Liu, H.; Hou, Y.; Niu, X.; et al. Diphenoquinone-Based Covalent Organic Frameworks for Efficient H_2O_2 Production via Photothermal Synergistic Catalysis. *Angew. Chem. Int. Ed.* **2026**, *65*, e9372067. https://doi.org/10.1002/anie.9372067.
46. Wang, Z.Q.; Zhu, Y.K.; Hu, Y.R.; et al. Local Electronic Modulation in Pillararene-Based Donor–Acceptor Conjugated Polymers for Selective Photocatalytic Oxygen Reduction. *Angew. Chem. Int. Ed.* **2026**, *65*, e9577048. https://doi.org/10.1002/anie.9577048.
47. Lu, J.; Qi, W.; Gu, S.; et al. Dual Metal-Bridged 2D COF for High Performance of H_2O_2 Photosynthesis across Wide pH Range Activated by Dual Route Linkage. *Angew. Chem. Int. Ed.* **2026**, *65*, e9931408. https://doi.org/10.1002/anie.9931408.
48. Peng, Y.; Yuan, L.; Liu, K.K.; et al. Photosynthesis of H_2O_2 using Phenothiazine-Based Covalent-Organic Frameworks Mimicking Coenzyme Q. *Angew. Chem. Int. Ed.* **2025**, *64*, e202423055. https://doi.org/10.1002/anie.202423055.
49. Zhao, W.; Li, Z.; Ren, G.; et al. Triphenylene-Derived Polyimide Covalent Organic Frameworks for Efficient Photosynthesis of Hydrogen Peroxide. *J. Am. Chem. Soc.* **2026**, *148*, 20647–20656. https://doi.org/10.1021/jacs.6c01900.
50. Tang, G.; Zhang, J.; Liang, G.; et al. Activating Triplet Excitons in COFs via Layer-Bridging Co Single Atoms for Photocatalytic H_2O_2 Production and Tandem C-N Coupling. *Angew. Chem. Int. Ed.* **2026**, *65*, e1580812. https://doi.org/10.1002/anie.1580812.
51. Li, Y.; He, J.; Lu, G.; et al. *De Novo* construction of amine-functionalized metal-organic cages as heterogenous catalysts for microflow catalysis. *Nat. Commun.* **2024**, *15*, 7044. https://doi.org/10.1038/s41467-024-51431-5.
52. Liu, F.; Hou, Y.; Wu, J.; et al. Spatially Manipulating Polar Centers of Covalent Organic Frameworks for Boosting Hydrogen Peroxide Photosynthesis and Water Purification. *Angew. Chem. Int. Ed.* **2026**, *65*, e2285238. https://doi.org/10.1002/anie.2285238.
53. Chen, S.X.; Cao, X.; Wang, M.; et al. Stepwise Conjugation Extension of Covalent Organic Frameworks via Multicomponent Linkage Conversion for Optimized Photocatalytic Molecular Oxygen Activation. *Angew. Chem. Int. Ed.* **2026**, *65*, e9207753. https://doi.org/10.1002/anie.9207753.
54. Li, Z.; Wang, Z.; Lan, D.; et al. Electronic Isolation Wall Engineering in Covalent Organic Frameworks for Enhancing Overall H_2O_2 Photosynthesis. *ACS Catal.* **2026**, *16*, 17456–17466. https://doi.org/10.1021/acscatal.6c05092.
55. Lin, H.; Tan, G.; Ju, Y.; et al. Thiophene-Doped Fully Conjugated Covalent Organic Frameworks for Efficient Photocatalytic Hydrogen Peroxide Generation. *CCS Chem.* **2026**, *8*, 1393–1406. https://doi.org/10.31635/ccschem.025.202506161.
56. Shu, C.; Yang, X.; Xie, P.; et al. Long-term photocatalytic hydrogen peroxide production by hydroquinone-buffered covalent organic frameworks. *Chin. J. Catal.* **2025**, *73*, 300–310. https://doi.org/10.1016/s1872-2067(25)64676-6.
57. Jiang, P.; Huang, Y.; Jiang, X.; et al. Revealing the Mechanism of Exciton Spontaneous Separation at Room Temperature for Efficient Photocatalytic Hydrogen Peroxide Synthesis. *Adv. Sci.* **2025**, *12*, e03929. https://doi.org/10.1002/advs.202503929.
58. Zhang, M.R.; Yuan, S.X.; Feng, Y.X.; et al. Heptazine-based conjugated microporous polymers for enhanced light absorption and charge separation in photocatalytic hydrogen peroxide production. *J. Mater. Chem. A* **2026**, *14*, 20173–20180. https://doi.org/10.1039/d6ta00689b. Correction in *J. Mater. Chem. A* **2026**. https://doi.org/10.1039/d6ta90296k.
59. Yan, H.; Jiang, J.; Huang, Y.; et al. Inter-Ring Bonding Electron Donor Structure Triggers Efficient Two-Electron Water Oxidation for Photocatalytic Hydrogen Peroxide Synthesis. *Adv. Mater.* **2026**, *38*, e07961. https://doi.org/10.1002/adma.202507961.
60. Yang, J.; Zhao, Z.; Liu, X.; et al. Homologous heteropolyaromatic covalent organic frameworks for enhancing photocatalytic hydrogen peroxide production and aerobic oxidation. *Nat. Commun.* **2025**, *16*, 7654. https://doi.org/10.1038/s41467-025-62937-x.